# Chaotic Organic Crystal Phosphorescent Patterns for Physical Unclonable Functions

*Healin Im, Jinsik Yoon, Jinho Choi, Jinsang Kim, Dong Hyuk Park*, Wook Park*, and Sunkook Kim**

Dr. H. Im, Prof. S. Kim
School of Advanced Materials Science and Engineering

Sungkyunkwan University, Suwon-Si, Gyeonggi-do, 16419, Republic of Korea

Email: seonkuk@skku.edu

J. Yoon, Prof. W. Park

Institute for Wearable Convergence Electronics, Department of Electronics and Information Convergence Engineering, Kyung Hee University, Deogyeong-daero, Giheung-gu, Yongin-si, Gyeonggi-do, 17104 Republic of Korea

Email: parkwook@khu.ac.kr;



This is the author manuscript accepted for publication and has undergone full peer review but has not been through the copyediting, typesetting, pagination and proofreading process, which may lead to differences between this version and the Version of Record. Please cite this article as doi: 10.1002/adma.202102542.

Prof. J. Kim

Department of Materials Science and Engineering, University of Michigan, Ann Arbor, Michigan 48109, United States

J. Choi, Prof. D. H. Park

Department of Chemical Enginerring , Program in Biomedical Science & Engineering, Inha University, 100 Inha-ro, Michuhol-gu, Incheon 22212, South Korea

Email: donghyuk@inha.ac.kr;

**KEYWORDS** Physical unclonable functions, organic crystal patterns, $MoS_2$, security labels

**Abstract**

Since the 4$^{th}$ Industrial Revolution, the Internet of things (IoT) based environments have been widely used in various fields ranging from mobile to medical devices. Simultaneously, information leakage and hacking risks also increase significantly, and secure authentication and security systems are constantly required. Physical unclonable functions (PUF) are in the spotlight as an alternative. We have developed chaotic phosphorescent patterns based on an organic crystal and atomic seed heterostructure for security labels with PUFs. The phosphorescent organic crystal patterns are formed on the $MoS_2$. They seem similar in macroscopic scales, whereas each organic crystal exhibits highly disorder features in microscopic scales. In image analysis, an encoding capacity as a single PUF domain achieves more than $10^{17}$ on a $MoS_2$ small fragment with lengths of 25 μm. Therefore,

security labels with phosphorescent PUFs could offer superior randomness and no-cloning codes, possibly becoming a promising security strategy of the authentication process.



## 1. Introduction

With the advances in smart technologies, artificial intelligence (AI) based smart Internet of things (IoT) environment is invigorated in various fields from mobile to medical devices. Accordingly, the security system with an anti-counterfeiting encryption key attracts tremendous demands to offer to tighten the protection of personal information and privacy[1–3]. To date, most secret keys and algorithms rely on software (SW) based encryption key management, which owns high risks of information extrusion. To overcome these weaknesses, hardware (HW) based encryption key management such as a physical unclonable function (PUF) has been spotlighted as a promising alternative strategy. PUF provides impregnable security keys through the disordered physical features derived from fabrication processes' deviations[4–10]. The consequent physical randomness could offer individual keys such as a unique fingerprint without external sources. Besides, it facilitates to implement with cost-effective and concise methods but a high level of security.

There have been numerous PUF methods proposed[11]. For example, static random access memory PUF (SRAM PUFs)[12,13] utilizes insecure programmed states caused by the program disturb errors as PUF signals. Optical PUF[4] exploits random speckle patterns attributed to the complicated interference by an inhomogeneous plastic shade. Edible PUF[14] performs counterfeit medicines with different fluorescent proteins. Besides, quantum dot PUF[15] demonstrates disordered flower-like

patterns derived from an inkjet-print process. However, these approaches of PUF emerge limitations in the aspect of information capacity and integration with the existing security system.

Regarding the design of PUFs, a strategy should guarantee high randomness, miniaturization, simple fabrication, and superior data collection speed. In this regard, scalable organic crystal patterns are a powerful potential candidate as a random number generator. Organic crystal patterns are facile to manufacture by simple solution-based processes, including inkjet printing[16,17], solution spin casting[18], and solution drop casting[19]. Under *in situ* crystallization process, organic molecules are site-specifically nucleated and crystallized by surface treatments on the substrates[20,21] to form the desired pattern on large scales. In contrast, individual organic crystals exhibit unexpected physical features such as size, morphology, and luminescence in micro scales, applicable for anti-counterfeiting encryption keys. Besides, each organic crystal pattern depends on the size of pre-defined area, possibly downsizing encryption keys and boosting the information capacity per unit area. Furthermore, simple spectrometers could observe organic crystal's luminescence characteristics with intuitive image analysis, enabling useful and high-speed data collection.

Herein, chaotic phosphorescent patterns are implemented by *in situ* crystallization of organic molecules and demonstrated for anti-counterfeiting codes of PUFs. Scalable $MoS_2$ films are synthesized by a two-step process[22] and pre-patterned as a square shape with each length of 25 μm. Two types of organic crystal patterns are formed by the solution drop-casting on the pre-patterned $MoS_2$ films. Organic molecules are preferentially nucleated and crystallized on $MoS_2$ owing to the surface energy differences between $MoS_2$ and substrate. In addition, $MoS_2$ can optimize photophysical features of organic crystals at room temperature. Both organic crystals on $MoS_2$ exhibit phosphorescent emission at room temperature under ultraviolet (UV) light irradiations.

Moreover, we have analyzed organic crystal micropatterns in digitization and cross-correlation to examine their randomness and encoding capacity as PUFs. For a precise analysis, the square-shaped $MoS_2$ pattern is defined as a unit area of a PUF. Furthermore, we have suggested the authentication processes of the proposed phosphorescent organic crystal patterns. As a result, it shows the potential to be the next generation PUFs as a core technology of encryption systems for the future.

## 2. Results and discussions

Chaotic phosphorescent PUFs are demonstrated based on the inherent random features of organic crystals by *in situ* crystallization. **Figure 1**a illustrates an outline of the proposed PUF strategy. Two-dimensional (2D) security labels such as a quick response (QR) code or a bar code are designed in macroscopic scales for general authentication processes. The desirable 2D labels are composed of microscopic-scale organic crystals site-specifically grown on atomic seeds. In image analysis, the luminescence characteristics of disordered organic crystals are examined under UV light irradiations and translated as anti-counterfeiting keys. It could offer double-encryption for the general security labels, readily boosting security safety. Besides, each signal is collected in the form of luminescence, assuring no interference from residual dust.

**Figure 1**b illustrates *in situ* crystallization-based fabrication processes of emissive organic crystal patterns. Large area $MoS_2$ films are formed by a two-step method[22] and patterned with a desirable design. Precursor solution with phosphorescent organic materials is drop-casted on as-prepared $MoS_2$ micropatterns and slowly evaporated under ambient conditions. In this work, 2,5-dihydroxyterephthalate (DDT) for green phosphorescence and 5-bromo-2,6-dihexyloxy-1-

naphthaldehyde (Np6A) and 1,5-dibromo-2,6-dihexyloxynapthalene (Np6) for red phosphorescence are utilized (see **Supporting Figure 1**)[23,24]. Note that $MoS_2$ micropatterns as atomic seeds could modulate organic crystal formation.

**Figure 1**c and d show charge-coupled device (CCD) images of DDT and Np6A/Np6 crystals on a single $MoS_2$ seed. Multiple organic crystals per $MoS_2$ seed are formed with random physical features such as size, shape, and location. We extract the features from the emission images and categorize them into 5 parameters: size, aspect ratio, orientation, position, and the number of crystals per $MoS_2$ seed. Area (*a*) is pixel components collected from the region where organic crystals emit light in the images. Then, a possible oval is assumed and calculated for each crystal. Based on the arbitrary ovals, aspect ratio (*r*), a minor axis/major axis ratio, and orientation (*o*) along the major axis are defined. The number of organic crystals per atomic seed (*n*) and the probability of *n* crystals ($P_n$) are also classified. Besides, a single $MoS_2$ seed is divided into 8 regions every 45 degrees, and the position (*p*) of organic crystals is categorized. These parameters are used to estimate the possible encoding capacity of organic crystals/$MoS_2$ patterns.

To form discrete organic crystal patterns, $MoS_2$ should be used as pre-defined atomic seeds for PUF domains. **Figure 2**a illustrates the two-step method of scalable $MoS_2$ films. A few nanometer-scale Mo film is deposited by an RF sputter and annealed with $H_2S$ gas at 1000 °C for 1 h, transforming Mo into $MoS_2$ films. The two-step grown $MoS_2$ films are characterized by Raman and X-ray photoelectron spectroscopies (**Figure 2**b and c). Raman spectrum of $MoS_2$ film emerges at 406.05 and 381.30 $cm^{-1}$ with a peak difference of 22.8 $cm^{-1}$, corresponding to the $A_{1g}$ and $E^1_{2g}$ modes of few-layer $MoS_2$[25]. According to the XPS analysis, $Mo^{4+}$ $3d_{5/2}$ and $S^{2-}$ $2p_{3/2}$ appear at 229.7 and 162.4 eV, revealing the covalent bonds of Mo and S. In addition, the atomic structures of the $MoS_2$ films are

examined by transmission electron microscopy (TEM). As shown in **Figure 2**d, the $MoS_2$ film is polycrystalline with multiple small grains of hexagonal lattice structures. In addition, partial Moirè patterns are attributed to the heterogeneity of the $MoS_2$ layer numbers.

**Figure 2**f to h show the optical images of $MoS_2$, DDT/$MoS_2$, and Np6A/Np6/$MoS_2$ patterns. It demonstrates the well-formed discrete organic crystal patterns. To elucidate the preferential organic crystalization on $MoS_2$, contact angle analysis is performed for DDT and Np6A/Np6 solutions, as shown in **Supporting Figure 2**a and b. Both solutions spread on the Si/$SiO_2$ substrate, resulting in undetectable contact angles. In contrast, DDT and Np6A/Np6 solutions show contact angles of 5.50 ± 0.5 ° and 6.56 ± 0.1°, respectively, on large-area $MoS_2$ films, denoting that the surface energy differences between substrate and $MoS_2$. The site-specifical growth of organic crystals may be attributed to the surface energy differences[20,26].

Moreover, it is observed that DDT crystals are site-specifically grown on different 2 dimensional (2D) materials such as $MoSe_2$, $WS_2$, and $WSe_2$ (**Supporting Figure 3**). To establish the interaction between DDT molecular alignment and 2D materials, DDT molecules on the graphene surface are explored by scanning tunneling microscopy (STM). In **Supporting Figure 4**, bright dots are occasionally attached to the well-arranged graphene honeycomb structure. These dots are benzene rings of DDT molecules, and the spacing between dots is possibly alkyl chain distances. This indicates that DDT molecules may be aligned along the graphene lattices. Considering this phenomenon, we assume that this would occur on the hexagonal lattice structures of $MoS_2$. As aforementioned, two-step grown $MoS_2$ films comprise abundant small grains, achieving the disorder crystallization of DDT with multiple orientations and positions on the $MoS_2$ domains.

Next, the organic crystals are examined in the aspect of photophysical properties. **Figure 3**a shows photoluminescence (PL) spectra of DDT and Np6A/Np6 with and without $MoS_2$ seeds. Intrinsic DDT crystals emit blue fluorescence at a wavelength ($\lambda_{em}$) of 468 nm, whereas that on $MoS_2$ seeds show a clear red-shift in PL peak with green phosphorescence at the $\lambda_{em}$ of 511 nm. Meanwhile, a PL spectrum of Np6A/Np6 shows a weak fluorescent component at around $\lambda_{em}$ of 449 nm and clear doublets at $\lambda_{em}$ of 591 and 634 nm corresponding to the phosphorescent components. On the contrary, the fluorescent component of Np6A/Np6 crystal is considerably reduced on $MoS_2$ seeds. Each emission color is marked in the Commission International de L'Eclairage (CIE) coordinate diagram, as shown in **Figure 3**b. The inherent emissions at (0.1648, 0.2096) for DDT and (0.4401, 0.3048) for Np6A/Np6 are significantly shifted to (0.2714, 0.5250) and (0.5194, 0.3881) along with $MoS_2$ seeds, respectively. Furthermore, time-resolved PL spectra are measured at room temperature, and their lifetimes are extracted as shown in **Figure 3**c and **Table 1**. Both types of organic crystals on $MoS_2$ exhibit extensive lifetimes as compared to pristine status.

We implement further analysis to elaborate on the variations in photophysical features of organic crystals on $MoS_2$. Low-temperature PL analysis is performed for DDT and DDT/$MoS_2$ to confirm the origin of abrupt green luminescence of DDT/$MoS_2$. Under low-temperature conditions, most organic molecules lose their molecular vibration and deactivate the vibrational energy loss, resulting in the activation of phosphorescence[27,28]. DDT is expected to suppress its molecular vibrations and promote the inherent phosphorescent features. **Supporting Figure 5**a and b present temperature-dependent PL spectra of DDT and DDT/$MoS_2$. In DDT, broad doublets, possibly deconvolute into two discrete peaks at approximately 446 and 543 nm, emerge at 77 K. A newly formed PL peak at 543 nm may be attributed to the phosphorescence activation of DDT. In DDT/$MoS_2$, PL spectra are constant

regardless of the surrounding temperature conditions, denoting that the phosphorescence of DDT is stabilized on $MoS_2$. Moreover, in Raman analysis (**Supporting Figure 5**c), DDT/$MoS_2$ shows a significant peak shift at approximately 1328 $cm^{-1}$ (marked as *), indicating $n\pi^*$ triplet states of C=O[29–31]. In Np6A/Np6 crystals, $MoS_2$ offers the ease condition for crystallization, stabilizing the red phosphorescences of Np6A/Np6 (**Supporting Figure 6**).

**Figure 3**d and e show CCD images of DDT/$MoS_2$ and Np6A/Np6/$MoS_2$ patterns. The luminescence images of organic crystal patterns achieve facile and intuitive image analysis. In these images, individual organic crystals are distinguishable from each other, readily sorting physical random features. In **Figure 3**d, most DDT crystals seem to be big and obtuse rhombohedron shapes. In **Figure 3**e, Np6A/Np6 crystals tend to show relatively small and random shapes. Moreover, Np6A/Np6 crystals own more individual fragments than the DDT crystals on a single $MoS_2$ seed. The macroscopic security labels seem almost identical from batch to batch, whereas the microscopic organic crystals are highly distinguishable and un-replicable. Such irregular micro-organic patterns are impossible to reproduce or copy.

Next, we have performed digitization analysis and 2D cross-correlation of chaotic phosphorescent patterns to evaluate the randomness and non-replicability. For high image analysis reliability, approximately 7,000 DDT and 3,000 Np6A/Np6 crystals (18k and 97k pixels, respectively) are collected and analyzed by a CCD camera. As shown in **Figure 4** and **Supporting Figure 7**, morphological features are mainly characterized into 5 parameters; area, aspect ratio, orientation, position, and the number of crystals per $MoS_2$ seed. These parameters are used as raw information to deduce the possible encoding capacity.

As shown in **Figure 4**, both DDT and Np6A/Np6 patterns show high randomness based on orientation and position with a flat distribution of 5.6 and 12.5 %. The remaining parameters (area, aspect ratio, and crystal number) exhibit clumped distributions. The orientation, position, crystal numbers, and probability are selected to extract the encoding capacity. The thresholds of orientations and position are 10° and 8 regions, respectively. In addition, we have extracted its possible random numbers in the ranges of more than 99 % of real cases. Therefore, the encoding capacity ($C_i$) on a single $MoS_2$ seed with 25 μm lengths could be estimated by the following equation,

$$C_i = p \sum_n P_n \times o^n$$

where *o*, *p*, *n*, *and* $P_n$ are the number of options derived from orientation, position, the number of crystals per $MoS_2$ seed, and the probability of forming *n* crystals. Thus, the producible $C_i$ is $6.116 \times 10^6$ for DDT and $2.744 \times 10^{17}$ for Np6A/Np6. Furthermore, if a security label is defined as an $A \times B$ array based on $MoS_2$ seeds, the group encoding capacity ($C_g$) could be exponentiated by the following equation.

$$C_g = (C_i)^{A \times B}$$

If a security label is designed in 1 $mm^2$ with abundant $MoS_2$ domains, $C_g$ is around $10^{2,700}$ and $10^{7,000}$ for DDT and Np6A/Np6, respectively, showing the commercialization potential as promising PUF applications.

Furthermore, 2D cross-correlation analysis has evaluated the uniqueness of DDT and Np6A/Np6 patterns. **Figure 5** presents the heatmaps and the histograms of cross-correlation values extracted from 480 4 × 4 DDT and 264 3 × 3 Np6A/Np6 PUF groups. In an identical crystal image (labeled as

intra-distance distribution), the correlation is high, and the coefficient value is close to 1. In different crystal images (labeled as inter-distance distribution), the coefficient value is nearly 0. In addition, the cut-off threshold and false positive/negative rates are calculated by applying the mean ($\mu$) and standard deviation ($\sigma$) to the Gaussian distribution function. **Table 2** to **7** present detailed values obtained from the cross-correlation of DDT and Np6A/Np6 patterns with different group sizes. 4 × 4 DDT group (**Figure 5**a and c) shows the false positive/negative rates of $5.248 \times 10^{-58}$ and $2.732 \times 10^{-55}$, while 3 × 3 Np6A/Np6 group (**Figure 5**b and d) is $2.430 \times 10^{-49}$ and $8.444 \times 10^{-49}$. Both groups are clearly divided with superior intercorrelation values, guaranteed as distinguishable patterns for PUF applications.

As aforementioned, conventional security labels such as QR codes or bar codes are designed with SW-based encryption algorithms. They are convenient and favorable for general authentication on macroscopic scales. However, SW-based labels are vulnerable to be counterfeited and stolen. On the contrary, security labels with un-replicable random microscale PUFs offer superior uniqueness and are nearly impossible to clone. We have proposed a highly secure and commercially available authentication process with phosphorescent PUF domains (**Figure 6**). At first, the desirable security labels with $MoS_2$ atom seeds are designed. Chaotic phosphorescent patterns based on organic crystals/$MoS_2$ are readily fabricated via solution drop-casting. As an image-based PUF manner, macro-patterns such as QR codes or logos are screened by bare eyes, and then the chaotic phosphorescent patterns role in double encryption keys. Pattern images are observed by affordable microscopic tools under UV light illumination. In evaluation, digitization and cross-correlation validate the randomness and estimate the encoding capacity of patterns. At this step, the images are obtained under different angles and distances to guarantee a decryption process. Each security label

with PUFs is saved and processed in an AI database. Consequently, during the decoding processes, the security labels could perform the general authentication process to validate whether the label is real or fake.

**3. Conclusions**

In conclusion, chaotic phosphorescent patterns are fabricated by *in situ* crystalization of pure organic crystals and demonstrated as anti-counterfeiting codes of PUFs. Organic molecules are site-specifically assembled and crystalized on $MoS_2$ seeds. Macroscopic phosphorescent patterns seem almost identical from batch to batch, whereas the microscopic organic crystals are highly distinguishable and un-replicable. This offers double-security by forming the desirable security labels consisting of small PUF domains. Moreover, we have performed digitization analysis and 2D cross-correlation of chaotic phosphorescent patterns to estimate the encoding capacity. From a single PUF domain, the producible encoding capacity is $6.11 \times 10^6$ and $2.74 \times 10^{17}$ for DDT and Np6A/Np6, respectively. This indicates that the security labels with phosphorescent PUFs could achieve superior randomness and the no-cloning codes, possibly commercializing. Therefore, chaotic phosphorescent patterns could be promising secure PUFs of the authentication process.

## 4. Experimental sections

### Preparation of phosphorescent organic crystal patterns

For $MoS_2$ seed atoms, large area $MoS_2$ are synthesized by a two-step process. At first, Mo film with a thickness of less than 2 nm is pre-deposited by RF sputter. The RF sputter and the deposition time are 150 W and 3 min, respectively. Then, Mo film is sulfurized by a gas phase sulfur precursor $H_2S$ at 1000 °C under the total gas flow condition of $H_2S$: $H_2$: Ar = 1: 50: 5, consequently forming uniform $MoS_2$ films. It is patterned as the desirable security label designs with small domains by photolithography.

For phosphorescent organic crystals, diethyl 2,5-dihydrocyterephthalate (97 %, from sigma Aldrich) is purchased and used without purification. 5-bromo-2,6-dihexyloxy-1-naphthaldehyde and 1,5-dibromo-2,6-dihexyloxynapthalene are synthesized. The precursor solutions are prepared by adding them into dimethylformamide with a 1 mg/ml concentration and stirring at room temperature before the solution drop-casting. To produce security labels with phosphorescent PUFs, the precursor solutions are dropped on the substrate with $MoS_2$ seeds under ambient.

### Characterization

Scalable $MoS_2$ films are examined by Raman spectrometer at $\lambda_{ex}$ of 514 nm and X-ray photoelectron spectrometer with a peak calibration at C 1s of 284.8 eV. A contact angle measurement observes the surface energy differences. A laser confocal microscope obtains photoluminescence and corresponding luminescent color-coupled device (CCD) images at $\lambda_{ex}$ of 405 nm. Time-resolved

photoluminescence (TRPL) measures organic crystals' lifetimes with impulse response function full-width half maximum of 240 ps at $\lambda_{ex}$ of 375 nm.

**Digitization analysis**

MATLAB software has proceeded for image analysis. At first, the green (0, 1, 0) and the red (1, 0, 0) filters extract the bright and the dark spots in luminescent images of DDT and Np6A/Np6 phosphorescent patterns. The threshold is defined by the 'graythresh' function and binarized with the 'im2bw' function. Here, objects less than 25-pixel size are removed with the 'bwareaopen' function to prevent residual dust influences. Then, individual organic crystals and the number of crystals per $MoS_2$ seeds are classified by the 'bwlabel' function. Besides, the 'regionprops' function elicits morphological features. It possesses various attribute values and properties; 'Area' for the region size, 'MinorAxisLength' and 'MajorAxisLength' for the aspect ratio, and 'Orientation' for the heading angle. For the location analysis where organic crystals are formed, thousands of extracted individual binary images are applied. The position probabilities are obtained for each location by calculating the average value through the 'mean' function after sorting and combining all the individual binarized images.

**Two-dimensional cross-correlation process**

A pattern should be perceived as identical even in different environmental conditions. Thus, each pattern is photographed twice for binarized images. In addition, it is demagnified by 5 times through the 'imresize' function. A weighted averaging filter is automatically applied by the 'bicubic' method as a default. By applying 3×3 size two-dimensional (2D) Kernel Filters, vertical ([-1 0 1; -2 0 2; -1 0 1]), horizontal ([-1 -2 -1; 0 0 0; 1 2 1]), and diagonal ([-2 -1 0; -1 0 1; 0 1 2], [0 -1 -2; 1 0 -1; 2 1 0])

orientation, in the 'conv2' function, the crystal edges are directionally classified. Then, it is analyzed by the 'normxcorr2' function and normalized cross-correlation method to determine the uniqueness.



**Acknowledgments**

This research is supported by the Basic Science Research Program through the National Research Foundation of Korea (NRF) (2021R1A2B5B02002167, 2021R1A4A5031805, 2021R1I1A1A01047275 and 2018R1A6A1A03025708).

**Competing interest**

The authors declare no competing interests.

**Reference**

[1] V. van der Leest, P. Tuyls, in *Des. Autom. Test Eur. Conf. Exhib. (DATE), 2013*, IEEE Conference Publications, New Jersey, **2013**, pp. 1137–1142.

[2] Z. Hu, J. M. M. L. Comeras, H. Park, J. Tang, A. Afzali, G. S. Tulevski, J. B. Hannon, M. Liehr, S.-J. Han, *Nat. Nanotechnol.* **2016**, *11*, 559.

[3] J. Zhang, K. L. McCann, C. Qiu, L. E. Gonzalez, S. J. Baserga, T. M. T. Hall, *Nat. Commun.* **2016**, *7*, 13085.

[4] R. Pappu, *Science (80-. ).* **2002**, *297*, 2026.

[5] M. R. Carro-Temboury, R. Arppe, T. Vosch, T. J. Sørensen, *Sci. Adv.* **2018**, *4*, e1701384.

[6] T. Takahashi, Y. Kudo, R. Ishiyama, in *2017 Fifteenth IAPR Int. Conf. Mach. Vis. Appl.*, IEEE, **2017**, pp. 202–206.

[7] R. Horstmeyer, B. Judkewitz, I. M. Vellekoop, S. Assawaworrarit, C. Yang, *Sci. Rep.* **2013**, *3*, 3543.

[8] B. Wigger, T. Meissner, A. Förste, V. Jetter, A. Zimmermann, *Sci. Rep.* **2018**, *8*, 4738.

[9] Y. Geng, J. Noh, I. Drevensek-Olenik, R. Rupp, G. Lenzini, J. P. F. Lagerwall, *Sci. Rep.* **2016**, *6*, 26840.

[10] R. Arppe, T. J. Sørensen, *Nat. Rev. Chem.* **2017**, *1*, 0031.

[11] Y. Gao, S. F. Al-Sarawi, D. Abbott, *Nat. Electron.* **2020**, *3*, 81.

[12] X. Xu, A. Rahmati, D. E. Holcomb, K. Fu, W. Burleson, *IEEE Trans. Comput. Des. Integr. Circuits Syst.* **2015**, *34*, 903.

[13] D. E. Holcomb, W. P. Burleson, K. Fu, *IEEE Trans. Comput.* **2009**, *58*, 1198.

[14] J. W. Leem, M. S. Kim, S. H. Choi, S.-R. Kim, S.-W. Kim, Y. M. Song, R. J. Young, Y. L. Kim, *Nat. Commun.* **2020**, *11*, 328.

[15] Y. Liu, F. Han, F. Li, Y. Zhao, M. Chen, Z. Xu, X. Zheng, H. Hu, J. Yao, T. Guo, W. Lin, Y. Zheng, B. You, P. Liu, Y. Li, L. Qian, *Nat. Commun.* **2019**, *10*, 2409.

[16] H. Minemawari, T. Yamada, H. Matsui, J. Tsutsumi, S. Haas, R. Chiba, R. Kumai, T. Hasegawa, *Nature* **2011**, *475*, 364.

[17] W. Wang, L. Wang, G. Dai, W. Deng, X. Zhang, J. Jie, X. Zhang, *Nano-Micro Lett.* **2017**, *9*, 52.

[18] Q. Wang, E. J. Juarez-Perez, S. Jiang, L. Qiu, L. K. Ono, T. Sasaki, X. Wang, Y. Shi, Y. Zheng, Y. Qi, Y. Li, *J. Phys. Chem. Lett.* **2018**, *9*, 1318.

[19] J. Jang, S. Nam, K. Im, J. Hur, S. N. Cha, J. Kim, H. Bin Son, H. Suh, M. A. Loth, J. E. Anthony, J.-J. Park, C. E. Park, J. M. Kim, K. Kim, *Adv. Funct. Mater.* **2012**, *22*, 1005.

[20] A. L. Briseno, S. C. B. Mannsfeld, M. M. Ling, S. Liu, R. J. Tseng, C. Reese, M. E. Roberts, Y. Yang, F. Wudl, Z. Bao, *Nature* **2006**, *444*, 913.

[21] H. Wang, F. Fontein, J. Li, L. Huang, L. Jiang, H. Fuchs, W. Wang, Y. Wang, L. Chi, *ACS Appl. Mater. Interfaces* **2020**, *12*, 48854.

[22] Y. Lee, J. Lee, H. Bark, I.-K. Oh, G. H. Ryu, Z. Lee, H. Kim, J. H. Cho, J.-H. Ahn, C. Lee, *Nanoscale* **2014**, *6*, 2821.

[23] O. Bolton, K. Lee, H.-J. Kim, K. Y. Lin, J. Kim, *Nat. Chem.* **2011**, *3*, 205.

[24] E. Cho, J. Choi, S. Jo, D. Park, Y. K. Hong, D. Kim, T. S. Lee, *Chempluschem* **2019**, *84*, 1130.

[25] A. K. Singh, P. Kumar, D. J. Late, A. Kumar, S. Patel, J. Singh, *Appl. Mater. Today* **2018**, *13*, 242.

[26] J. Liu, C. Zhu, K. Liu, Y. Jiang, Y. Song, J. S. Francisco, X. C. Zeng, J. Wang, *Proc. Natl. Acad. Sci.* **2017**, *114*, 11285.

[27] E. Sawicki, H. Johnson, *Microchem. J.* **1964**, *8*, 85.

[28] D. R. Kearns, W. A. Case, *J. Am. Chem. Soc.* **1966**, *88*, 5087.

[29] H. Ma, H. Yu, Q. Peng, Z. An, D. Wang, Z. Shuai, *J. Phys. Chem. Lett.* **2019**, *10*, 6948.

[30] F. Kobayashi, R. Ohtani, S. Teraoka, M. Yoshida, M. Kato, Y. Zhang, L. F. Lindoy, S. Hayami, M. Nakamura, *Chem. – A Eur. J.* **2019**, *25*, 5875.

[31] A. M. J. van Eijk, G. B. Ekelmans, W. Klinkenberg, A. H. Huizer, C. A. G. O. Varma, *J. Chem. Soc. Faraday Trans.* **1990**, *86*, 2083.

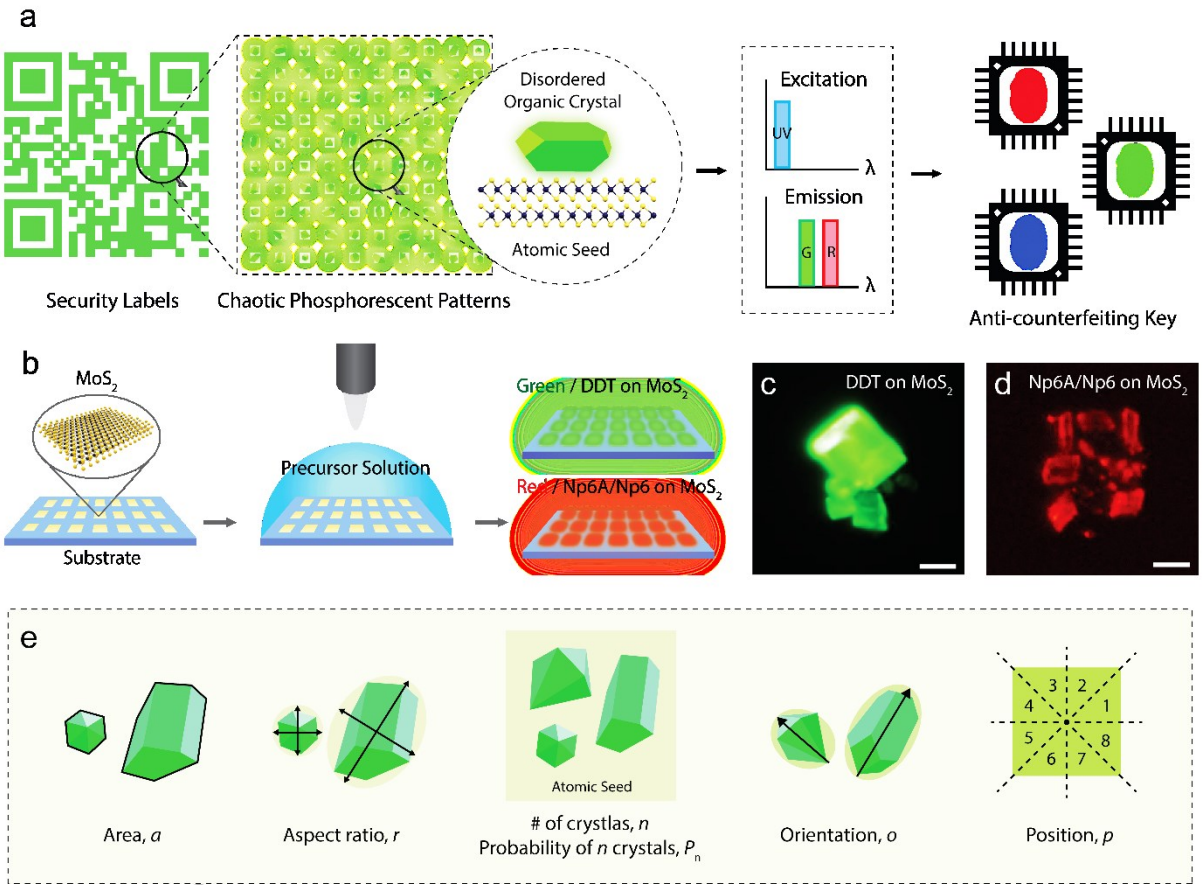


**Figure 1.** Outline of chaotic phosphorescent patterns for physical unclonable function (PUF). a) The Proposed PUF strategy with the disordered phosphorescent organic crystal patterns. b) Overall fabrication process. CCD images of pure organic crystals of c) DDT and d) Np6A/Np6 on $MoS_2$ (scale bar: 10 μm). e) Parameter classification in organic crystals for digitization analysis.

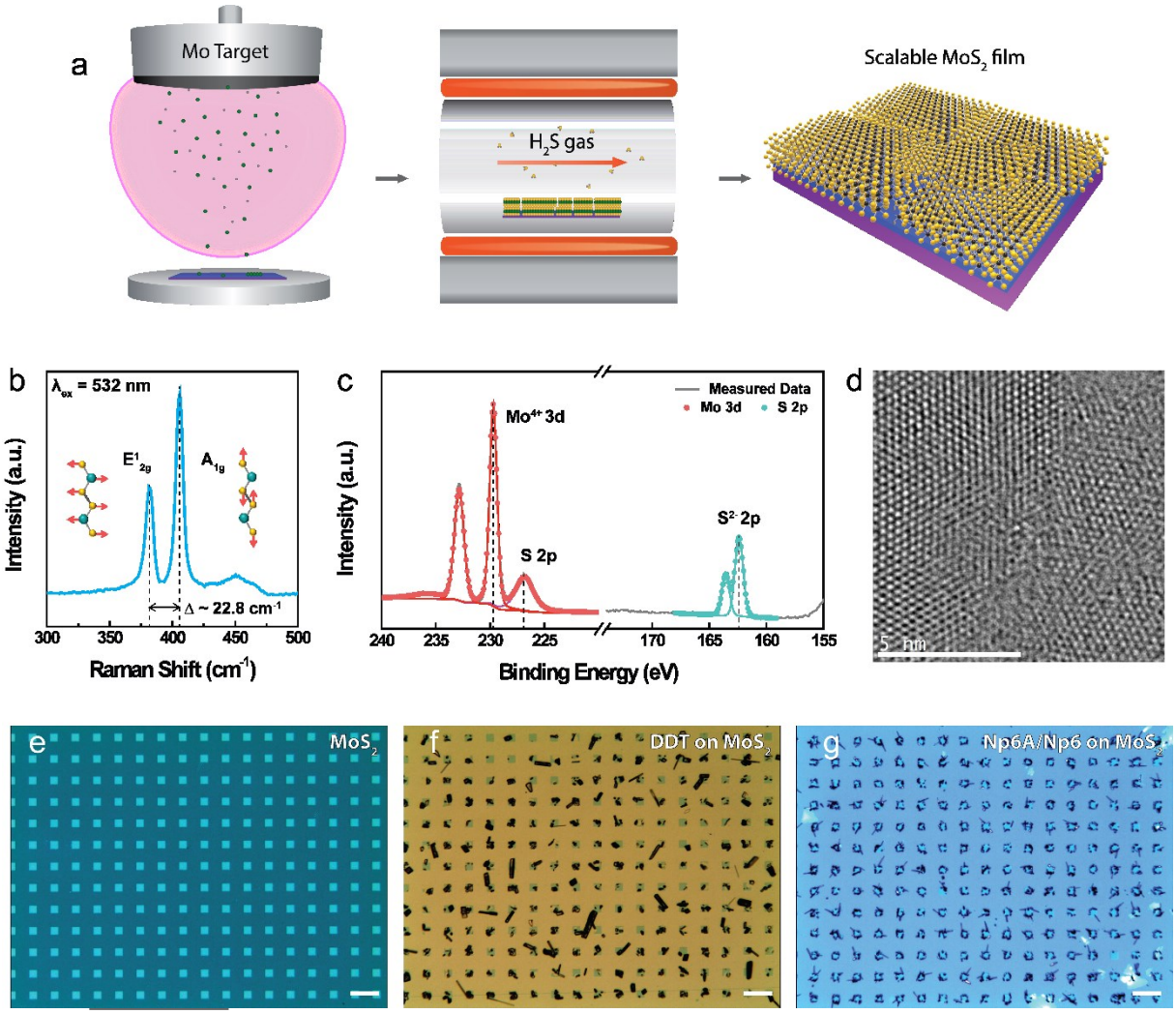


**Figure 2.** Scalable $MoS_2$ film. a) Two-step fabrication process. b) Raman analysis. c) XPS analysis. d) TEM image of $MoS_2$ film in plan view. Optical images of e) the patterned $MoS_2$, f) DDT on $MoS_2$, and g) Np6A/Np6 on $MoS_2$ (scale bar: 100 µm).

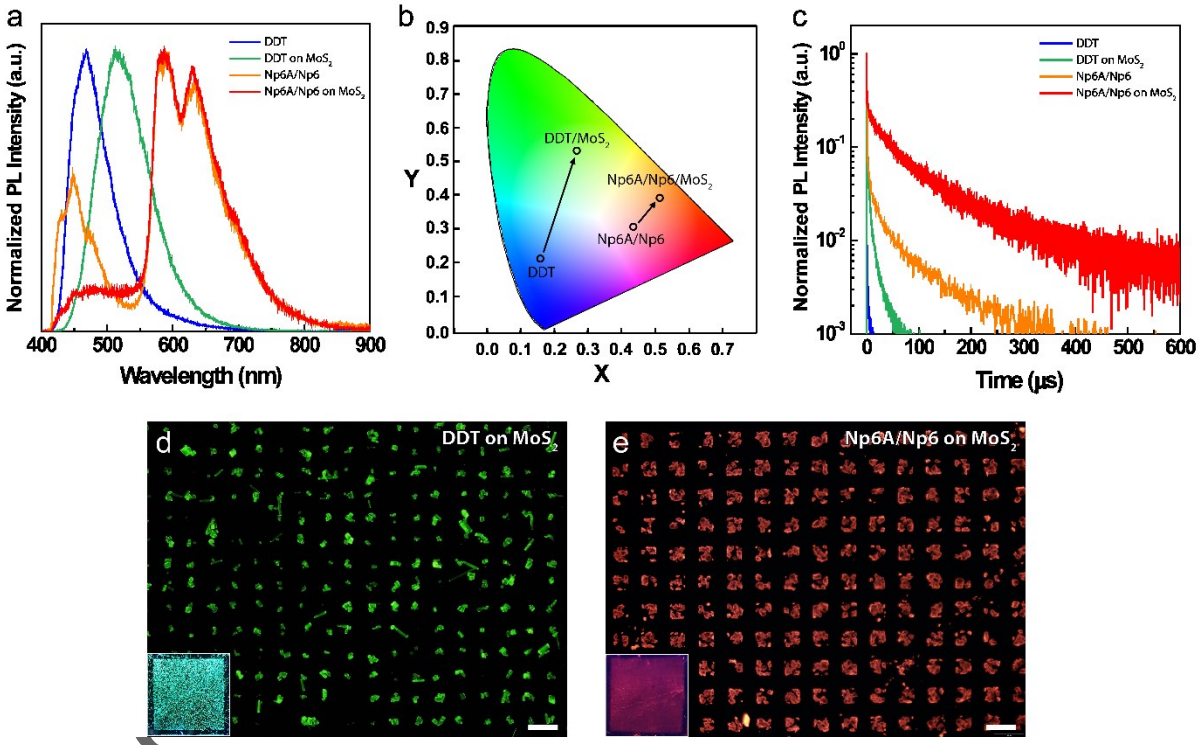


**Figure 3.** Photophysical properties of phosphorescent organic crystals. a) PL analysis, b) CIE chromaticity diagram, and c) time-resolved PL analysis of DDT, DDT on $MoS_2$, Np6A/Np6, and Np6A/Np6 on $MoS_2$. CCD images of d) DDT and e) Np6A/Np6 phosphorescent patterns (scale bar: 100 μm). Insets of d, e) are photographs of DDT and Np6A/Np6 patterns under a 365 nm lamp.

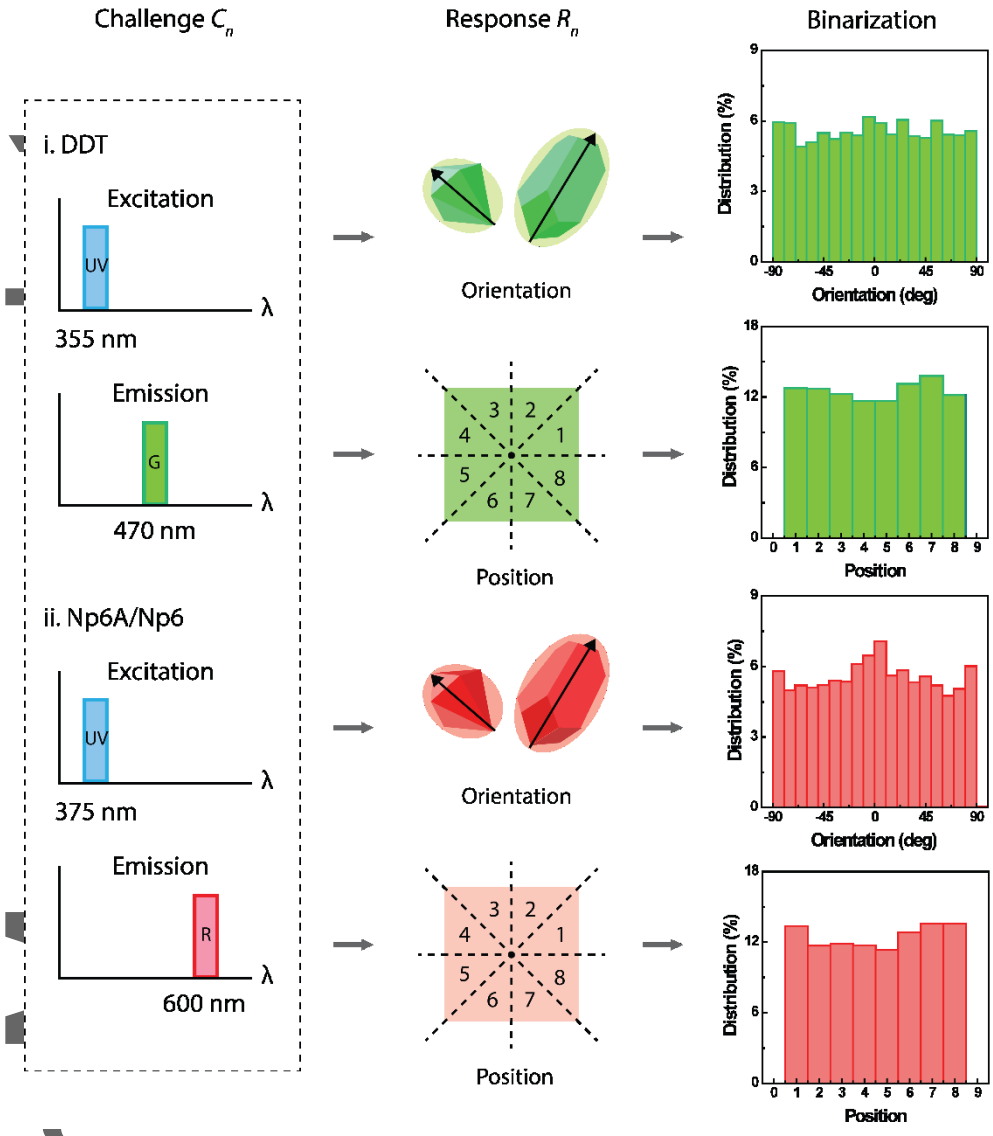


**Figure 4.** Flowchart of image analysis of chaotic phosphorescent patterns. At first, DDT and Np6A/Np6 crystals emit phosphorescence at wavelengths of 470 nm and 600 nm under UV light illumination. Based on orientation and position of chotic phosphrescent patterns, the randomness and the possible encoding capacity are statistically estimated.

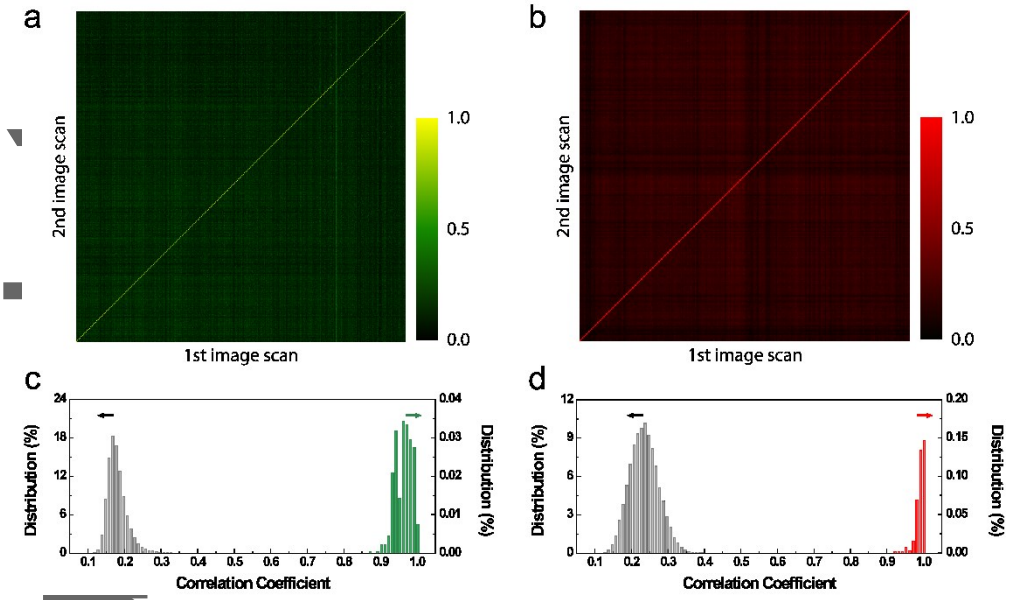


**Figure 5.** Heat maps and histograms of 2D cross-correlation values extracted from a, c) DDT and b, d) Np6A/Np6 patterns. Total data is obtained from 480 sets of 4 × 4 groups for DDT and 264 sets of 3 × 3 groups for Np6A/Np6.

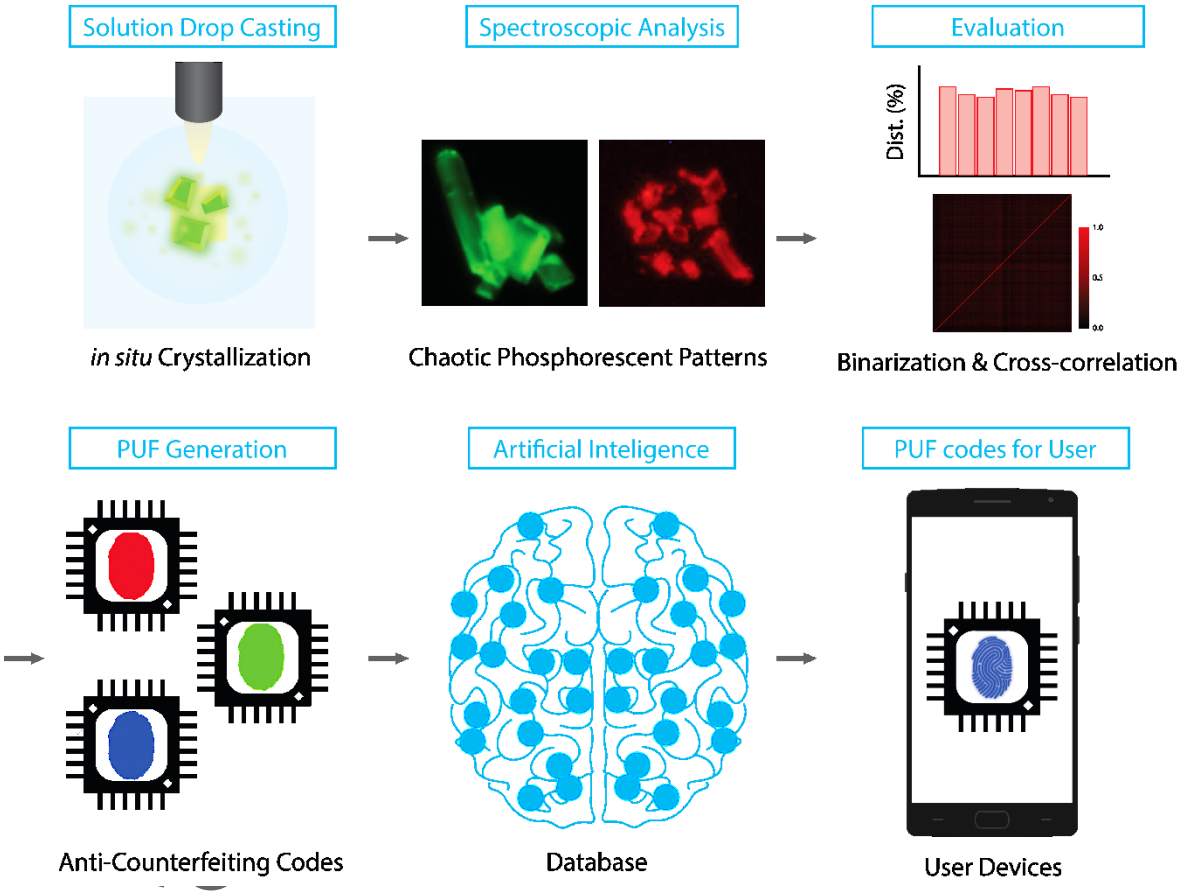


**Figure 6.** Proposed authentication process using chaotic phosphorescent pattern PUFs.

| Components | $\lambda_{ex}$ [nm] | $\lambda_{em}$ [nm] | Life-time [μs] |
|---|---|---|---|
| DDT | 355 | 470 | < 1.27 |
| DDT on $MoS_2$ | 355 | 530 | 9.27 |
| Np6A/Np6 | 375 | 600 | 86.17 |
| Np6A/Np6 on $MoS_2$ | 375 | 600 | 96.79 |

**Table 1.** Room temperature lifetimes of organic crystals. The excitation wavelength ($\lambda_{ex}$) and emission wavelength ($\lambda_{em}$) are selected according to PL spectra.

| Group size | 1×1 | 2×2 | 3×3 | 4×4 | 5×5 |
|---|---|---|---|---|---|
| (samples) | (959) | (1,098) | (880) | (480) | (300) |
| Mean($\mu$) | 0.4866 | 0.3014 | 0.2160 | 0.1770 | 0.1513 |
| Standard deviation($\sigma$) | 0.0716 | 0.0451 | 0.0313 | 0.0263 | 0.0244 |

**Table 2.** Inter-distance distribution of DDT patterns.

| Group size | 1×1 | 2×2 | 3×3 | 4×4 | 5×5 |
|---|---|---|---|---|---|
| (samples) | (959) | (1,098) | (880) | (480) | (300) |
| Mean($\mu$) | 0.9314 | 0.9476 | 0.9554 | 0.9559 | 0.9561 |
| Standard deviation($\sigma$) | 0.0248 | 0.0219 | 0.0235 | 0.0229 | 0.0223 |

**Table 3.** Intra-distance distribution of DDT patterns.

| Group size | 1×1 | 2×2 | 3×3 | 4×4 | 5×5 |
|---|---|---|---|---|---|
| (samples) | (1,099) | (768) | (264) | (132) | (88) |
| Mean($\mu$) | 0.3316 | 0.2457 | 0.2327 | 0.2295 | 0.2332 |
| Standard deviation($\sigma$) | 0.0444 | 0.0397 | 0.0391 | 0.0364 | 0.0339 |

**Table 4.** Inter-distance distribution of Np6A/Np6 patterns.

| Group size | 1×1 | 2×2 | 3×3 | 4×4 | 5×5 |
|---|---|---|---|---|---|
| (samples) | (1,099) | (768) | (264) | (132) | (88) |
| Mean($\mu$) | 0.9852 | 0.9853 | 0.9843 | 0.9845 | 0.9847 |
| Standard deviation($\sigma$) | 0.0188 | 0.0134 | 0.0121 | 0.0108 | 0.0108 |

**Table 5.** Intra-distance distribution of Np6A/Np6 patterns.

| Group size | 1×1 | 2×2 | 3×3 | 4×4 | 5×5 |
|---|---|---|---|---|---|
| Cut-off threshold | 0.8128 | 0.7352 | 0.6379 | 0.5939 | 0.5719 |
| False positive rate | $1.585\times10^{-7}$ | $1.511\times10^{-23}$ | $3.844\times10^{-43}$ | $5.248\times10^{-58}$ | $4.222\times10^{-68}$ |
| False negative rate | $3.293\times10^{-4}$ | $3.199\times10^{-20}$ | $4.537\times10^{-40}$ | $2.732\times10^{-55}$ | $1.458\times10^{-65}$ |

**Table 6.** Cut-off threshold and false positive/negative rates of DDT patterns.

| Group size | 1×1 | 2×2 | 3×3 | 4×4 | 5×5 |
|---|---|---|---|---|---|
| Cut-off threshold | 0.7898 | 0.7978 | 0.8055 | 0.8115 | 0.8030 |
| False positive rate | $1.150\times10^{-25}$ | $1.034\times10^{-44}$ | $2.430\times10^{-49}$ | $3.106\times10^{-58}$ | $5.826\times10^{-64}$ |
| False negative rate | $3.428\times10^{-25}$ | $3.619\times10^{-44}$ | $8.444\times10^{-49}$ | $1.186\times10^{-57}$ | $1.747\times10^{-63}$ |

**Table 7.** Cut-off threshold and false positive/negative rates of Np6A/Np6 patterns.

ToC Text

We have developed chaotic phosphorescent patterns based on an organic crystal and $MoS_2$ heterostructure for PUFs. The phosphorescent patterns on $MoS_2$ seem similar in macroscopic scales, whereas each organic crystal exhibits highly disorder features in microscopic scales. In image analysis, an encoding capacity as a single PUF domain achieves more than $10^{17}$ on a $MoS_2$ small fragment.